Dexterous manipulation planning of 3D miniaturized objects by four robotized probes in the presence of adhesion forces

Ivan Tchouatat Kepseu[1†], Tala Dannawi Aissaoui[1†], Michaël Gauthier[1], Redwan Dahmouche[1]

[1]Université Marie et Louis Pasteur, SUPMICROTECH, CNRS, institut FEMTO-ST, F- 25000, Besançon, France.

Contributing authors: tala.dannawi@femto-st.fr;
[†]These authors contributed equally to this work.

Abstract

This paper introduces a novel framework for optimal dexterous manipulation of 3D micro-objects with complex shapes through four robotized probes. The framework utilises a geodesic polyhedron sphere sampling method within the objects' configuration space to construct original graphs of interconnected stable, accessible, and collision-free grasps. The impact of this sampling method on the generated probe paths was evaluated, with performance assessed in terms of cost and time efficiency. To ensure robust manipulation paths, a worst-case scenario approach was adopted, where the dominant and time-varying adhesion forces at the micro-scale were overestimated when acting as a disturbing factor and disregarded when contributing to stabilisation. The A* algorithm was employed to generate complete and optimal manipulation probe paths. The simulation results demonstrated, for the first time, collision-free manipulation planning of miniaturised 3D objects with complex shapes in the presence of adhesion forces.

Keywords: Dexterous manipulation, robotic micro-assembly, path planning

1 Introduction

Many industrial [1] [2] and medical [3] [4] applications, such as micro-assembly or minimally invasive surgeries, require precise micro-manipulation tasks. Several solutions have been proposed in the scientific literature to manipulate micro-objects by adopting contact-based and

non-contact manipulation strategies [5]. Non-contact manipulation can be achieved through various approaches such as magnetic [6] [7], dielectrophoresis [8], acoustic [9], and thermocapillary forces [10]. However, non-contact manipulation methods typically suffer from low blocking forces, which limit their application possibilities. Conversely, contact-based micro-manipulation has the advantage of inducing high and localised forces.

Nevertheless, contact-based micro-manipulation still suffers from low dexterity because current solutions are not able to combine 6 Degrees of Freedom (DoF) micro-manipulation, large rotation angles, and high precision [11]. Indeed, serial robots can typically achieve high dexterity, but their precision is limited [12], while parallel architectures allow for high precision but with low dexterity [13]. One of the promising approaches to improve dexterity and achieve high precision is to perform in-hand micro-manipulation [14]. Unlike robots with simple micro-grippers, micro-manipulation with multiple probes would additionally allow for the manipulation of different object shapes. However, generating dexterous manipulation paths is still a challenge at both the macro-scale and the micro-scale [15]. Furthermore, the predominance of adhesion forces (van der Waals, electrostatic, and capillarity) over weight and inertial forces at the micro-scale makes micro-manipulation even more challenging [16].

At the macro-scale, dexterous manipulation is performed using learning methods [17][18] and planning methods [19]. Learning methods involve training robotic hands on specific objects experimentally or in simulated environments and then experimentally validating them [20]. Learning methods rely on fixed manipulation conditions, such as the coefficient of friction. This approach poses a problem at the micro-scale, as the interaction between the end-effector's tip and the micro-object is significantly affected by changes in temperature and humidity, or by the accumulation of electric charges on the surfaces of either the manipulated micro-objects or the the end-effector's tip. Approaches that are robust to these variations must therefore be considered. This is why planning methods are preferred over learning methods at the micro-scale [21].

Planning methods for dexterous manipulation are mainly based on two distinct approaches: i) probabilistic, such as Rapidly Exploring Random Trees (RRT) [22] and Probabilistic Roadmaps (PRM) [23], and ii) deterministic, such as A* and Dijkstra [24] [25]. At the micro-scale, the A* algorithm [26] and RRT* [27] have been used for micro-assembly applications. However, both manipulation methods had limited dexterity because: i) no out-of-plane rotations were performed; ii) the rotation ranges were limited; and iii) the objects' shapes were simple. To achieve larger rotation ranges, a finger gaiting strategy was proposed in [28]. It allowed for unlimited rotation ranges but was limited to planar manipulation. This method was extended to 3D manipulation by decomposing 3D rotations into successive 2D rotations using Euler angles [29]. However, since the rotation axes were limited to two, the generated manipulation paths were too constrained, inducing a high failure rate and paths with high costs. In [30], more optimal paths were generated thanks to a greater number of rotation axes that better covered the configuration space of the object. However, the manipulation planning was more complex due to the larger configuration space of the object. One question that arises is whether it is possible to generate more efficient manipulations by covering the configuration space of the manipulated object with a smaller number of rotation axes.

This question is similar to the problem of designing a transportation road-map for a city, where the objective is to connect different locations in the most efficient way given a certain cost. In this analogy, the locations represent the configurations of the manipulated object

in space (from the initial to the final one), the roads represent the rotation axes, and the construction cost represents the computational cost. Since any change in the rotation axis induces an acceleration, the challenge is to efficiently cover the object's configuration space with the least number of rotation axes.

In this work, we propose the first micro-manipulation framework that considers micro-objects with complex 3D shapes, the adhesion forces that exist at the micro-scale, and collision avoidance between the probes and the object, as well as between the probes themselves. We build upon the proof of concept presented in [31], which demonstrated micro-manipulation using three beams, each with 2 DoF, to achieve 2D rotations as shown in Fig. 1. Specifically, we extend the approach to achieve 3D rotations around multiple axes using a system of four probes, three for grasping and one dedicated to finger-gaiting, where each probe has 3 DoF.

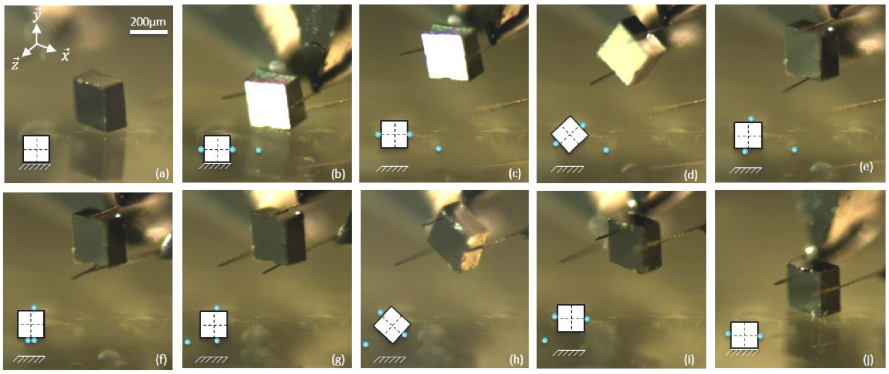

Fig. 1: Experimental in-hand planar manipulation of a 220 μm silicon square using three fingers. The object is firstly detached from the substrate (a→c). Then, a first rotation is performed (c→e). After the in-hand regrasping (e→g), a second rotation (g→i) enables the tested 180°reorientation, finally replacing the object on the substrate (i→j). [31].

This article also extends and enhances the work presented in [30], mainly by introducing an original and more efficient sampling method of the configuration space in terms of the number of rotational axes and computational cost. It also integrates inter-probe collision avoidance and is more versatile as it has been extended to 3D objects with complex shapes. Therefore, this paper offers, for the first time, a comprehensive framework for performing manipulation of complex 3D micro-objects in the presence of adhesion forces by having four probes.

In Section 2, we present the modelling and background of robotic micro-manipulation, while in Section 3, we tackle the problem of probe-object collision by assessing the accessibility of each of the probe to the object and by measuring the achievable rotation ranges. In Section 4, we explain the methodology used to sample the configuration space and build a graph necessary for optimal path planning using the A* algorithm. Section 5 presents the obtained simulation results and their analysis. Finally, Section 6 provides a conclusion and discusses the main perspectives.

2 Modeling and Background

2.1 Manipulation System

We consider a system composed of four co-micromanipulation probes. Each probe has a fixed orientation and 3 DoF in translation (XYZ), with a motion range significantly larger than the size of the manipulated object. The probes have conical shapes with an opening angle φ and axis $\mathbf{v_k}$, as shown in Fig. 2. Their sharp tips allow us to neglect the rolling of the manipulated objects on the probes. The probes are localised in the reference frame $\mathcal{R}(\mathbf{x}, \mathbf{y}, \mathbf{z})$, which is attached to the workspace.

We assume that the weight of the objects is negligible, as is often the case in micromanipulation. Knowing that a minimum of three probes is needed to stabilise and rotate objects in space, the manipulation process will consist of a succession of 3D rotations and "finger gaiting" when required [32]. Although the four probes do not properly represent a hand, we use the term '"finger gaiting" to refer to the placement of one tool tip (or probe) and the detachment of another one while the object is kept stable in the same orientation. During the entire manipulation process, the probes continuously ensure eligible grasps of the manipulated object.

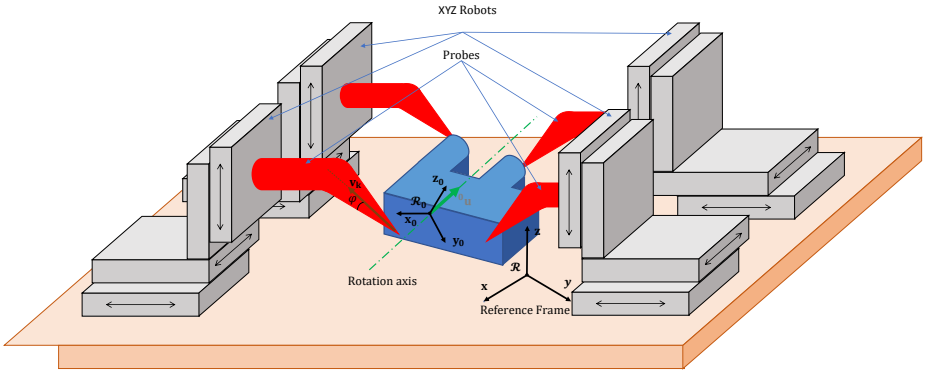

Fig. 2: Illustration of the micromanipulation architecture composed of four translating conical probes

A grasp is considered eligible if: i) the grasp is stable, and ii) the probes can reach the contact points on the object without any collision between them or with the object. Both criteria are detailed in the following sections.

2.2 Stable Grasp Condition

Let us consider a rigid object in contact with n_f rigid probes. The k^{th} probe applies a force $\mathbf{f}_k$ at a point P_k, which lies within the friction cone defined by the normal of the object's surface $\mathbf{n}_k$ at the contact point and the friction coefficient μ. The presence of the pull-off force $\mathbf{f}_{po}$ allows the object to be pulled to a certain extent, which leads to a modified friction cone as

shown in Fig. 3. The forces that can be applied by each probe in the presence of the pull-off forces (or adhesion forces) must lie within the modified friction cone [33].

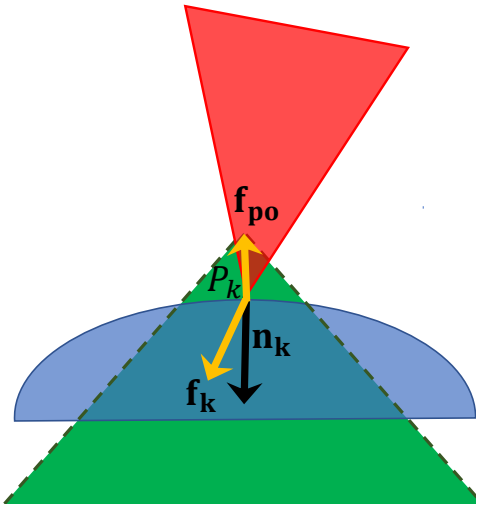

Fig. 3: Interaction forces between the probes and the manipulated object. The contact force at point P_k lies within the friction cone defined by the contact point P_k, the normal vector of the object's surface at the contact point $\mathbf{n}_k$, and the amplitude of the pull-off force.

Considering O as the origin of the frame attached to the object and assuming static equilibrium, the sum of the wrenches applied by each probe represented at O implies that:

$$\sum_{k=1}^{n_f} \boldsymbol{W}_k + \boldsymbol{W}_{ext} = 0 \; ; \tag{1}$$

where $\boldsymbol{W}_k$ is the wrench generated by the force $\mathbf{f}_k$, which contributes to the grasp, and $\boldsymbol{W}_{ext}$ is the wrench of external forces.

When a probe is detached from the object, it no longer contributes to the grasp, and a pull-off force between the object and the tool tip induces a disturbing external wrench ($\boldsymbol{W}_{ext} = \boldsymbol{W}_{po}^{\mathrm{d}}$). Before considering detaching a probe, one must ensure that the remaining ones can resist such a disturbing wrench, as represented in Fig. 4. The grasp is thus stable if all the forces applied by the remaining probes lie within their respective friction cones.

3 Probe Accessibility and Rotation Ranges

3.1 Accessibility

The contact between the probes and the object is limited to the probe's tip only. Since the probes translate but do not rotate, the unit vectors $\mathbf{v}$, which define the orientations of the conical probes, are also constant. To simplify the accessibility assessment of the probe to the

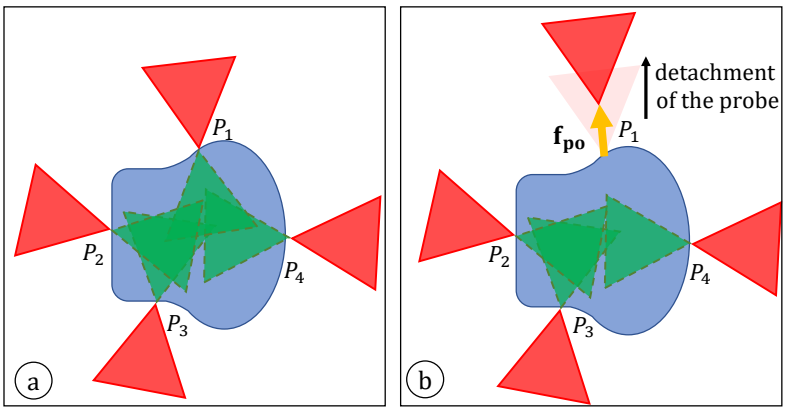

Fig. 4: A 4-probe grasp (a) with the friction cone of each probe and (b) the detachment of a probe at the point P_1, which applies a pull-off force that the remaining probes should withstand.

object and avoid probe-object collision, we limit the contact points to the flat and convex surfaces. This condition is satisfied if the tangential plane at the contact point does not intersect the object. The total number of contact points n_c is subject to a compromise. Indeed, increasing n_c would improve the grasping and manipulation possibilities but would also increase the computation time. Objects with flat surfaces are sampled around regular positions while guaranteeing a minimum distance between the samples. For non-planar shapes, the selection of the contact points is random, while also considering a threshold distance between them. The contact points are thus accessible if the angle between the probe's axis $\mathbf{v}$ and the tangent plane at the contact point is greater than the half-angle of the cone φ. To prevent any risk of collision, we can also define the admissible angle $\varphi_l = \varphi + \Delta\varphi$, where $\Delta\varphi$ represents a safety margin between the probes and the object. This is visualised in Fig. 5.

The accessibility condition can then be expressed as follows:

$$\mathbf{v} \cdot \mathbf{n} \geq \sin(\varphi_l); \tag{2}$$

We also consider the risk of collision between the probes. Since the probes are represented as cones, we sample points on one cone and verify if they are outside the surface of another cone. Let the cone $\mathcal{C}$ have apex O, semi-angle ϕ, and height h, attached to frame $\mathcal{R}_\mathcal{C}(O, \mathbf{x}, \mathbf{y}, \mathbf{z})$. For point P with coordinates (x_p, y_p, z_p) in frame $\mathcal{R}_\mathcal{C}$ to be outside cone $\mathcal{C}$, one of three conditions should be respected for each sampled point on the probe to ensure that there is no collision:

i. Outside the surface of the other cone;
ii. Behind the apex of the other cone.

Condition 1: Let P' be the projection of P onto cone $\mathcal{C}$. The distance $d_{PP'}$ from P to the cone axis is defined as:

$$d_{PP'} = \sqrt{x_p^2 + y_p^2} \tag{3}$$

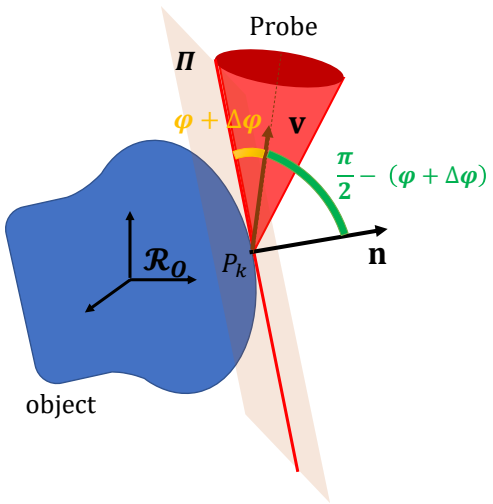

Fig. 5: Accessibility of the contact point if the angle between the probe's axis $\mathbf{v}$ and the tangent plane at the contact point is greater than the half-angle of the cone φ, taking into account a safety margin $\Delta\varphi$.

Let M be the intersection of the lateral surface of the cone with PP', as shown in Fig. 6. The distance $d_{MP'}$ from M to the cone axis is defined as:

$$d_{MP'} = z_p \tan(\phi) \tag{4}$$

For P to be outside the lateral surface of the cone, the following condition must be respected:

$$d_{MP'} < d_{PP'} \tag{5}$$

Condition 2: As shown in Fig. 7, P is behind the apex of the cone if:

$$\mathbf{OP'} \cdot \mathbf{z} < 0 \tag{6}$$

A grasp is eligible if it is stable, every probe can access the object (2), and there is no collision between the probes (5) and (6).

3.2 Probe-Object Collision-Free Rotation Ranges

Given the accessibility condition in (2), one can calculate the admissible rotation range of an object when it is in contact with a probe. Although the orientation of the probes is fixed in the global frame while the object rotates, the probes appear to rotate when viewed from the object's frame. To determine the rotation limit, let us consider the relative rotation of the probe observed from the object's frame. The new orientation of the probe in the object's frame $\mathbf{v'_{lim}}$ after a rotation of θ_{lim} of the object around the axis $\mathbf{u}$ can be expressed as follows using Rodrigues' formula:

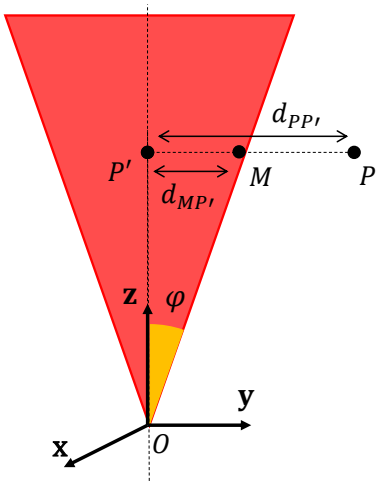

Fig. 6: Condition 1 for probe-probe collision: P on the outer lateral surface of the cone.

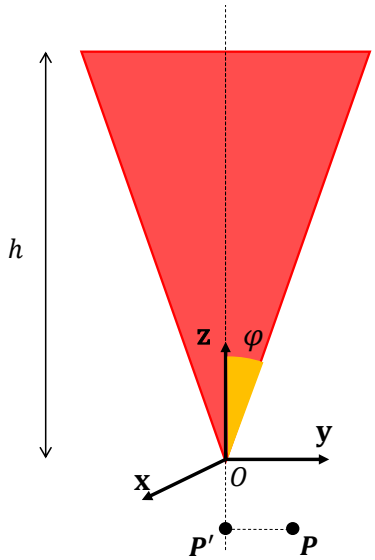

Fig. 7: Condition 2 for probe-probe collision: P behind the apex of the cone.

$$\begin{aligned}\mathbf{v'}_{lim} =& \mathbf{v}\cos(\theta_{lim}) + (\mathbf{u}\wedge\mathbf{v})\sin(\theta_{lim}) \\ &+ \mathbf{u}(\mathbf{u}\cdot\mathbf{v})(1-\cos(\theta_{lim}))\end{aligned} \tag{7}$$

The rotation angle corresponding to the accessibility limit can be directly deduced from (2):

$$\mathbf{n} \cdot \mathbf{v'}_{lim} = \sin(\varphi_l) \tag{8}$$

Substituting $\mathbf{v'}_{lim}$ expressed in (7) into (8) and rearranging the coefficients, we obtain the following system of equations where θ_{lim} is the unknown:

$$\alpha \cos(\theta_{lim}) + \beta \sin(\theta_{lim}) = \gamma \tag{9}$$
$$\text{with} \begin{cases} \alpha = \mathbf{n} \cdot \mathbf{v} - (\mathbf{n} \cdot \mathbf{u})(\mathbf{u} \cdot \mathbf{v}) \\ \beta = \mathbf{n} \cdot (\mathbf{u} \wedge \mathbf{v}) \\ \gamma = \sin(\varphi_l) - (\mathbf{n} \cdot \mathbf{u})(\mathbf{u} \cdot \mathbf{v}) \end{cases}$$

This system of equations has four solutions: two positive and two negative. In Fig. 8, θ_1 and θ_2 are the positive solutions, which correspond to the minimum and maximum angles for the probe's accessibility on the object. On the other hand, θ_3 and θ_4 are the negative solutions of the equation, which correspond to the probe being located inside the object. Therefore, only positive solutions are admissible. The rotation range can thus be expressed as an interval bounded by the rotation limits $\Delta\theta_k = [\theta_1, \theta_2] = [\theta_{min}, \theta_{max}]$.

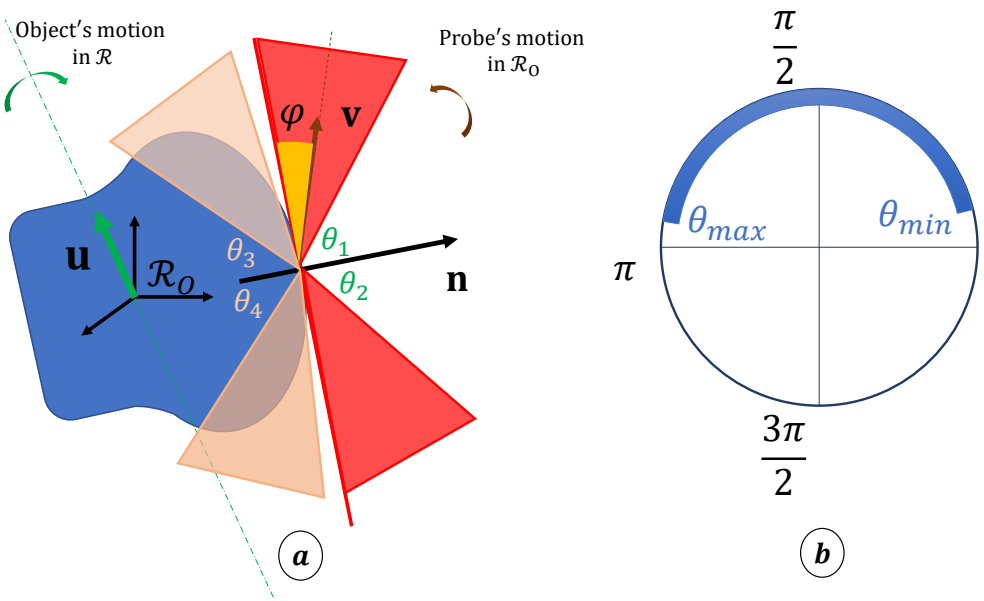

Fig. 8: Illustration of the rotation range caused by the probe-object collision. In (a), the configuration of the probe is represented in the object frame $\mathcal{R}_o$ when it has reached the accessibility limit. (b) represents the rotation interval $\Delta\theta = [\theta_{min}, \theta_{max}]$, where θ_{min} and θ_{max} are the limit angles reached by the probe at the accessibility limit of the object.

3.3 Probe-Probe Collision-Free Rotation Ranges

To determine the rotation range induced by the probe-probe collision around the axis $\mathbf{u}$, we divide the entire rotation range of the object around the axis $\mathbf{u}$ (of 2π) into several small rotation ranges of $\delta\theta$. We then check if the condition from (5) and (6) is respected at the start and end configurations of each rotation step of $\delta\theta$. Then, the feasible object's rotation range $\Delta\theta_{kk'}$ around $\mathbf{u}$, considering the possible collision of probes k and k', can be expressed as follows:

$$\Delta\theta_{kk'} = \cup\left(\delta\theta_{free}\right); \tag{10}$$

where $\delta\theta_{free}$ is the set of collision-free rotation intervals for each involved probe.

Since all the probes used in a grasp must meet the accessibility and collision-free conditions, the rotation range of one grasp $\Delta\theta_{grasp}$ around an axis $\mathbf{u}$ is conditioned by the intersection of all the admissible rotation ranges of the involved probes:

$$\Delta\theta_{grasp} = \Delta\theta_1 \cap \cdots \cap \Delta\theta_{12} \cap \cdots \cap \Delta\theta_{n_f-1 n_f} \tag{11}$$

After obtaining the set of stable and collision-free grasps of the object, the next step is to interconnect them and navigate in the resulting graph to perform the dexterous micromanipulation with the four probes.

4 Dexterous micromanipulation planning method

Moving the object in translation is straightforward since it requires exactly the same translation of all the probes. As there is no relative motion between the probes and the object or between the probes themselves, the problem of stable translation is reduced to the problem of a stable grasp. Therefore, we can decouple the translations from the rotations. Both operations can thus be superimposed, given the motion range of the probes. Consequently, in the manipulation planning, we focus more on the rotation of the objects, which is much more challenging.

In order to perform trajectory planning for dexterous micromanipulation, we build a graph $\mathcal{G}$ that contains all the eligible grasps for all configurations of the object as nodes, interconnected by two types of edges: rotations (different object configurations but the same grasp) and finger gaiting (the same configuration of the object but different grasps).

4.1 Graph Building

Any graph is built from nodes and edges. We define the nodes N_i as the combination of an orientation of the object ${}^0\mathbf{R}_i$ and an eligible grasp G: $N_i = \{{}^0\mathbf{R}_i, G_i\}$. Each grasp G_i contains the indices of the contact points p_{ij} of the probes on the object, where $j = 1, ..., 4$:

$$N_i = \begin{cases} {}^0\mathbf{R}_i \\ G_i = \quad [p_{i1}, p_{i2}, p_{i3}, p_{i4}] \end{cases} \tag{12}$$

Since only one probe can be located at a given contact point, they must be different in each grasp ($p_{i1} \neq p_{i2} \neq p_{i3} \neq p_{i4}$). A special index, such as zero, can be assigned to a probe that is not used in the grasp.

The edges in the graph represent the connections between the nodes. Since a node is constructed from the combination of an orientation and a grasp, any change in the object orientation or grasp would lead to a different node. Considering two configurations (or orientations) ${}^0\mathbf{R}_i$ and ${}^0\mathbf{R}_j$, the direct rotation ${}^i\mathbf{R}_j$ between both can be defined as:

$$ {}^i\mathbf{R}_j = rot({}^i\mathbf{u}_j, \theta_{i,j}) \tag{13} $$

where ${}^i\mathbf{u}_j$ is the rotation axis and $\theta_{i,j}$ is the rotation angle. If there is a *three*-probe grasp G allowing for the direct rotation ${}^i\mathbf{R}_j$, respecting the stability conditions in (1) and avoiding collision (meaning θ_{ij} is included in $\Delta\theta_{grasp}$ defined in (11)), then $G_i = G_k$ and the nodes $N_i = \{\mathbf{R}_i, G_i\}$ and $N_j = \{\mathbf{R}_j, G_j\}$ are connected with a rotation edge.

Considering the same configurations ${}^0\mathbf{R}_i$ and ${}^0\mathbf{R}_j$, if the *three*-probe grasps G_i and G_k have two probes at the same contact points (e.g. $p_{i1} = p_{j1}$ & $p_{i2} = p_{j2}$), and the third used probe is different (e.g. $p_{i3} \neq 0$ & $p_{j3} \neq 0$), then it is possible to switch between the grasps G_i and G_j. We first attach the probe p_{j4} to obtain an intermediate *four*-probe grasp, and then we detach the probe p_{i3}. The pull-off force of the removed probe disturbs the grasp, while the adhesion forces of the remaining probes contribute to stabilising the grasp. To generate reliable and robust manipulation paths, we consider the worst-case scenario where the disturbance is maximal and the stabilisation is minimal. This means that the pull-off force of the removed probe is at its maximum, while the adhesion forces of the remaining probes are null. Considering this worst-case scenario, the three remaining probes of G_j must resist the pull-off force due to the detachment of the probe p_{i3} as expressed in (1). If this condition is satisfied, the nodes defined by $N_i = \{{}^0\mathbf{R}_i, G_i\}$ and $N_j = \{{}^0\mathbf{R}_i, G_j\}$ are linked with a finger gaiting edge. The interconnection of the nodes will result in the micro-manipulation planning graph, which takes into account the adhesion forces at the micro-scale. However, we still need to define the object's configuration space sampling strategy, which is explained in the next section.

4.2 Sampling Approaches of the 3D Rotational Space

Before tackling the problem of the 3D rotational configuration space, let us make an analogy with the 3D translation configuration space. A regular and homogeneous sampling of a normal volume would be a 3D grid. In this case, all the distances between the grid's nodes would be equal and any displacement between two nodes on the grid would involve just two perpendicular translations. Angular acceleration, which requires moving at a low speed, would be experienced at most twice when changing directions between the three translation axes. This is why the road systems in many modern cities are arranged in this way.

It would be interesting to have an equivalent sampling when performing rotations. Unfortunately, it is more complicated to regularly sample the rotational configuration space since, unlike translations, it is not a linear space. In addition, any change of rotational axis would lead to an acceleration inducing non-smooth manipulation. An efficient sampling that addresses these issues would: i) be able to cover all the 3D rotation space, and ii) minimise the change in rotational axes when rotating from one configuration to another.

In fact, orientations can be represented as positions inside a sphere, and the sampling of the rotational configuration space can be represented as the sampling of the volume of a sphere. Several sphere sampling methods have been developed. However, they have not

yet been used in robotic dexterous manipulation. A sphere can be sampled through random sampling methods, but these would require a large number of rotation axes to cover the whole configuration space. In [34], a modified random sampling algorithm was used for sphere sampling for visibility computation, while in [35] random sampling was used in an RRT* by limiting the search area to a sphere or an ellipsoid. Although these methods were able to achieve quasi-uniform sampling of the configuration space, they did not take into account the constraint of aligning the samples on the same rotation axes. In [36], a statistically uniform distribution of orientations was developed on a sphere for path planning purposes. However, it was not homogeneous.

Another sampling approach is the Discrete Global Grid System (DGGS), which partitions the surface of a sphere into a discrete set of cells. The longitude-latitude sphere sampling is one of the most commonly used DGGS [37], which is based on lines of longitude (vertical lines from pole to pole) and lines of latitude (horizontal circles around the sphere). However, it is not homogeneous since the sampling density increases towards the poles [38], which can also lead to singularities [39].

Geodesic DGGS, on the other hand, uses regular polyhedra with equilateral triangular faces. The polyhedron is subdivided into smaller triangles recursively [40]. Icosphere and octasphere sampling methods are examples of geodesic DGGS that start with an icosahedron or octahedron [41], which have 20 or 8 equilateral triangular faces, respectively. We will refer to icosphere sampling and octasphere sampling as $icosampling$ and $octasampling$ respectively. $Icosampling$ provides more uniformly distributed axes compared to $octasampling$ since it is based on a polyhedron with a higher number of faces. $Icosampling$ and $octasampling$ are used in several applications, such as computer vision and medical imaging [42] [43], but have not yet been used for dexterous manipulation. Also, they are normally used to sample the volume instead of the surface of a sphere, as required in dexterous manipulation.

4.3 The Proposed Sampling Approach

The method we propose to produce an efficient sampling of the object configuration space is to use Geodesic DGGS to generate interconnected successive samples on concentric sphere surfaces, as shown in Fig. 9.a. The process starts from a home configuration, which can be the identity matrix ${}^0\mathbf{R}_0$, and is repeated at each generation n. This results in $\mathbf{R}_{i_n}$ configurations at each generation, with $\mathbf{R}_{i_n}$ being the configuration $\mathbf{R}_i$ that results after applying the rotation at generation n. The rotations are applied from the initial orientation, as shown in Fig. 9.b-f. Expressed relatively to the initial configuration, the rotations ${}^0\mathbf{R}_{i_n}$ are defined as follows:

$$ {}^0\mathbf{R}_{i_n} = rot({}^0\mathbf{u}_{i_n}, n \times \theta_{samp}) \tag{14} $$

where ${}^0\mathbf{u}_{i_n}$ are the unit vectors representing the rotation axes defined in ${}^0\mathbf{R}_0$ and θ_{samp} is a rotation angle. Starting from a first set of rotation axes ${}^0\mathbf{u}_{i_1}$ for the first generation, new unit vectors are generated at each new generation. The set of rotation axes in generation $(n+1)$ are derived from the axes of rotation in generation n by either $icosampling$ or $octasampling$. Both $icosampling$ and $octasampling$ methods create polyhedral approximations of a sphere, starting from an icosahedron or octahedron respectively and using a different initial set of ${}^0\mathbf{u}_{i_n}$. The process of $octasampling$ is illustrated in Fig. 9, where at the first generation, 6

vertices are created, which correspond to 6 configurations. The angle between two neighbouring axes is $90°$ in the first generation. $Icosampling$ follows the same process, however, 12 rotational axes are created with an angle of $63.43°$ between neighbouring axes in the first generation. As n increases, the polyhedron is refined by subdividing its faces into smaller triangles, thus increasing the number of vertices (i.e. configurations). For example, for $n = 2$, using $octasampling$, 18 vertices are created, which would be closer to the outer surface of the sphere, and the angular distance between neighbouring axes decreases to $45°$ as shown in Fig. 9-c.

The interconnections between the vertices are created for neighbouring configurations either belonging to the same generation n or to two successive generations, n and $n + 1$. We consider that two configurations generated by the rotations ${}^0\mathbf{R}_{i_n}$ and ${}^0\mathbf{R}_{j_m}$, with m being n or $n + 1$, are adjacent if the angle between their generating axes respects the following condition:

$$\cos\left(\frac{\lambda}{2^n}\right) \leq {}^0\mathbf{u}_{i_n} \cdot {}^0\mathbf{u}_{j_m} \tag{15}$$

where λ is the angle between two adjacent rotation axes used in the first generation (i.e. $90°$ in $octasampling$ and $63.43°$ in $icosampling$), and $\frac{\lambda}{2^n}$ is the angle between the rotation axes for configurations i and j in generation n. As n increases, the angle between the generating axes ($\frac{\lambda}{2^n}$) decreases, i.e. they become closer to each other. This is why the more generations we have, the more the condition of determining adjacency becomes strict, and only configurations with very close generating axes would be considered adjacent. This is expressed through the inequality in (15), where ${}^0\mathbf{u}_{i_n} \cdot {}^0\mathbf{u}_{j_m}$ is the angle between the two rotation axes.

4.4 Path Planning Strategy

The micromanipulation planning related to the rotation part consists of finding the optimal path from an initial orientation $\mathbf{R}_{ini}$ to a final one $\mathbf{R}_{fin}$ in the constructed graph $\mathcal{G}$. It is very unlikely that the initial or the final configurations correspond to one of the samples. Consequently, both the initial and the final configurations are added to the configuration space after verifying that it is admissible.

Let us consider N_{ini} and N_{fin}, two nodes corresponding to $\mathbf{R}_{ini}$ and $\mathbf{R}_{fin}$, as shown in Fig. 10.b. Planning for the manipulation consists of generating a path between N_{ini} and N_{fin} in the modified graph $\mathcal{G}'$ where the two new configurations have been added, as represented in Fig. 10.c. The A* algorithm is then used to explore the graph and generate the optimal path. The algorithm minimises the evaluation function $f(N_i)$ defined as follows:

$$f(N_i) = h(N_i) + g(N_i) \tag{16}$$

where $g(N_i)$ is the cost function from the initial node to the current node N_i, and $h(N_i)$ is the heuristic function, which evaluates the cost function from the current node to the final one without overestimating it. Therefore, the cost function $g(N_i)$ at the node $N_i = [{}^0\mathbf{R}_i, G_i]$ linked with the node $N_j = [{}^0\mathbf{R}_j, G_j]$ depends on the cost of the parent node $g(N_{previous})$ and the type of edge between them:

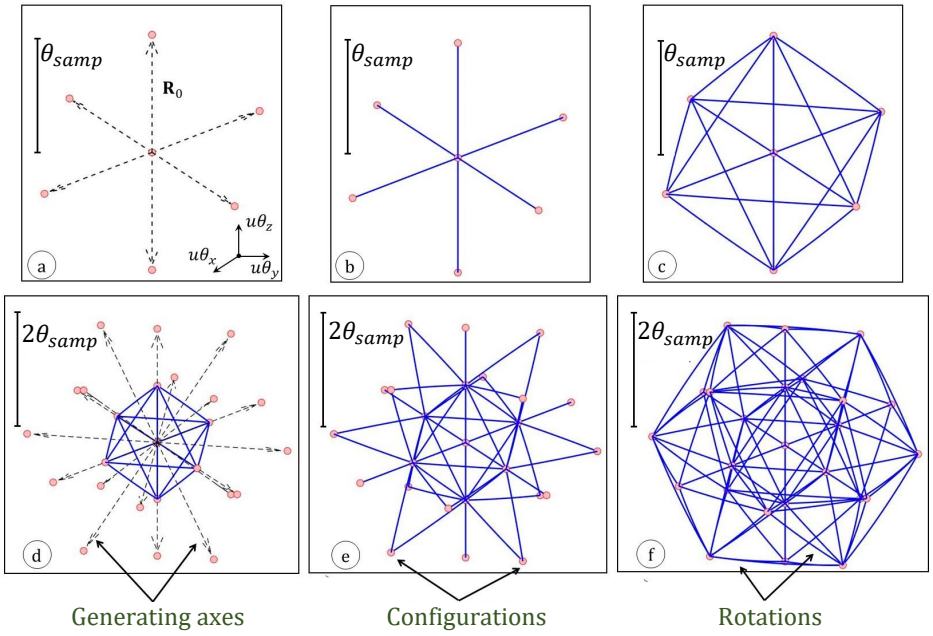

Fig. 9: Illustration of the sampling method $octasampling$ for the first two generations of configurations and the interconnection between them. (a) The start configuration $\mathbf{R}_0$, and the configurations $\mathbf{R}_{i_{(1)}}$ of the generation $n = 1$ obtained after rotations of $\theta_{samp} = \frac{\pi}{6}$ around 6 generating axes. (b) Connection of the first generation's configurations with $\mathbf{R}_0$. (c) Interconnection of the configuration $\mathbf{R}_{i_{(1)}}$ to their neighbours inside the same generation, they are considered neighbours if the angle between their generating axis is $\lambda = \frac{\pi}{2}$. (d) The generation $n = 2$ also starting from $\mathbf{R}_0$, obtained after rotations of $2\theta_{samp} = \frac{\pi}{3}$. (e) Connection of the generation $n = 2$ with the generation $n = 1$. (f) Interconnection of the neighbouring configurations in generation $n = 2$, knowing that the neighbourhood relation now is $\frac{\lambda}{2} = \frac{\pi}{4}$.

- Case of rotation: the cost is equal to the angle between the parent ${}^0\mathbf{R}_i$ and child ${}^0\mathbf{R}_j$, leading to the cost:

$$g(N_j) = g(N_i) + \theta_{ij} \tag{17}$$

- Case of finger gaiting: The added cost is g_g, corresponding to a fixed value. The cost function is updated as follows:

$$g(N_j) = g(N_i) + g_g \tag{18}$$

Considering a current node $N_i = [\mathbf{R}_i, G_i]$, we define the heuristic function as the angle of the direct rotation from the current to the final node N_{fin}:

$$h(N) = \theta_{i\,fin} \tag{19}$$

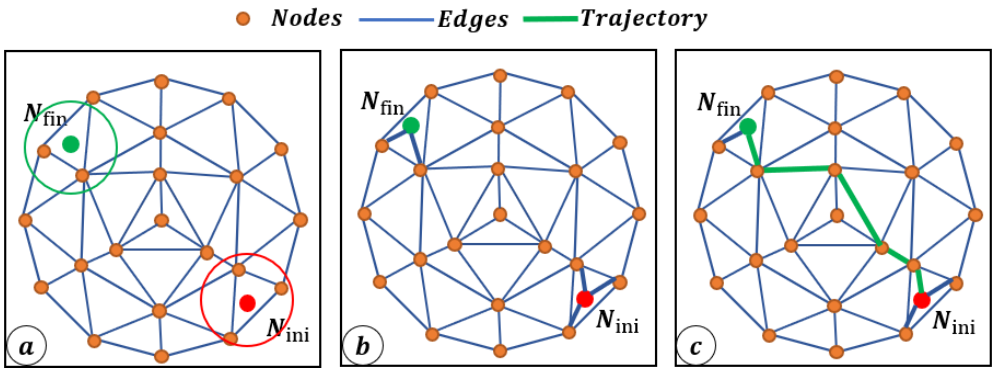

Fig. 10: Illustration of the path planning strategy: (a) The precomputed graph $\mathcal{G}$, the initial (resp. final) nodes in red (resp. green), and the circle representing the space that contains the nearest nodes belonging to the graph $\mathcal{G}$. (b) Connection of $\mathbf{N}_{ini}$ & $\mathbf{N}_{fin}$ to $\mathcal{G}$, and transformation of $\mathcal{G}$ into $\mathcal{G}'$. (c) The search for the optimal trajectory from the nodes $\mathbf{N}_{ini}$ to the nodes $\mathbf{N}_{fin}$ in $\mathcal{G}'$.

Thanks to the constructed graphs, the heuristics, and the cost function, the A* algorithm allows optimal paths to be generated for dexterous micromanipulation. The complexity of the manipulation planning depends on the complexity of the graph. Large graphs would lead to better manipulation paths but at the expense of computational cost.

5 Simulation results and analysis

In this section, we present and assess the simulation results of the proposed manipulation planning framework by verifying the effectiveness of the proposed sampling method, its impact on the generated trajectories, as well as the impact of adhesion forces for the multi-probe dexterous micromanipulation. All the simulations were conducted in MATLAB®, running on a system with the following characteristics: Windows 10, Intel(R) Core(TM) $i5-10310U$ CPU $[1.70-2.21]$ GHz, 16 GB RAM.

We considered the two complex objects illustrated in Fig. 11. We sampled their surfaces with $n_{c1}=44$ and $n_{c2}=41$ contact points respectively for objects (1) and (2). The system is composed of four identical conical probes. The opening angle of the cones is $\varphi=\frac{\pi}{6}$ and the safety margin is $\Delta\varphi=\frac{\pi}{20}$. We chose the same friction coefficient for both objects $(\mu=0.5)$. We assumed that the magnitude of the pull-off force is $f_{po}^{\mathrm{d}}=0.5\mu N$, and the maximum grasping force is $f_k=1\mu N$. We set the cost of finger gaiting equal to half a turn $(g_g=\pi)$.

The selected contact points for Object (a) and Object (b) are shown in Fig. 12 along with examples of invalid contact points that did not meet the condition of the minimum threshold distance or where the tangential plane at the point cut through the object.

5.1 Sampling of the Object's Configuration Space

To sample the object's configuration space, we applied two variations of geodesic DGGS introduced in Section 4.2, namely *octasampling* and *icosampling*. The difference between

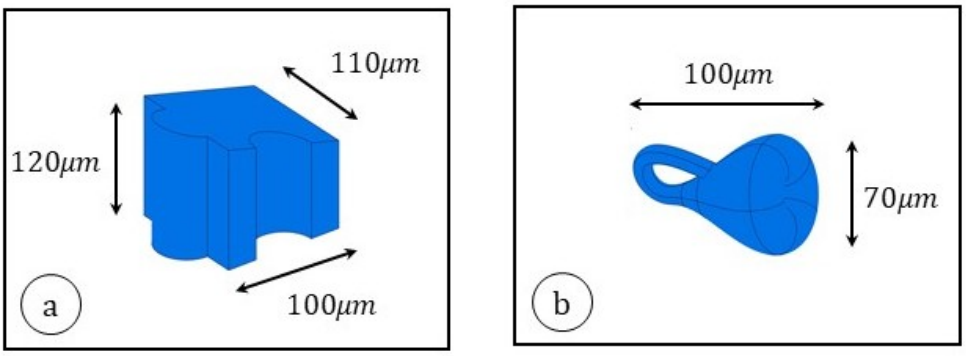

Fig. 11: Objects used in simulation. (a) Object (a), (b) Object (b).

Table 1: Graph properties for Object (a) to study the impact of the sampling method.

Object (a)	Graph $\mathcal{G}_1$	Graph $\mathcal{G}_2$
Sampling	Icosampling	Octasampling
Adhesion	None	
Nodes	632 822	286 147
Rotation edges	2 925 440	962 559
Re-grasping edges	6 755 592	3 191 641

the two lies in the starting polygon and the axes at each generation (or layer), which lead to a different distribution and orientation of points. The angle between two generations is $\theta_{samp} = \frac{\pi}{6}$ for both, and there are $n = 4$ generations. Using $icosampling$, the number of possible rotations is 8076 and the number of rotation axes is 321, while for $octasampling$, we obtained 3240 elementary rotations and 129 rotation axes. Therefore, $octasampling$ has fewer rotations since it has a larger angle between the adjacent rotation axes λ. On average, the same rotation axis generated around 12 rotations in both $icosampling$ and $octasampling$, considering that each axis has a positive and a negative direction. They both generate the same number of rotations due to the fact that both methods have the same number of generations. The standard deviation of the angles between the samples is similar (0.15) using $icosampling$ and $octasampling$. This index is much higher in uniform random sampling using Euler angles (0.85) and quaternions (0.65) [36], indicating that the sampling method we proposed is more homogeneous.

5.2 Impact of the Sampling Method

We generated the stable and admissible grasps and sampled the objects' configuration spaces using the two proposed methods, which allowed us to generate the manipulation graphs $\mathcal{G}_1$ and $\mathcal{G}_2$ for both objects, based respectively on $icosampling$ and $octasampling$. The properties of $\mathcal{G}_1$ and $\mathcal{G}_2$ are presented in Table 1. Initially, we did not take adhesion forces into

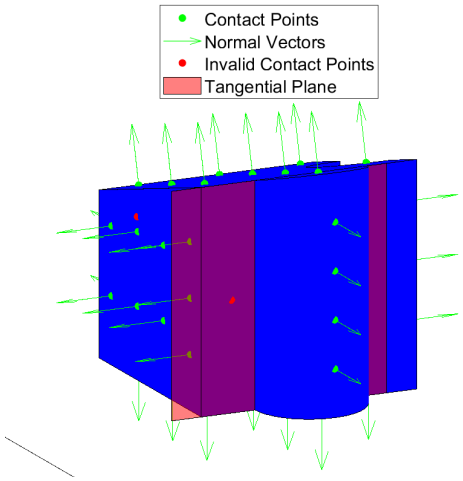

(a) Contact points of Object (a)

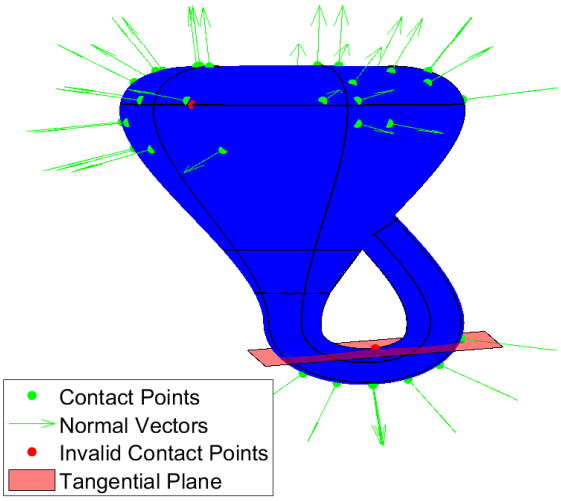

(b) Contact points of Object (b)

Fig. 12: Selected contact points and examples of invalid contact points due to the tangential plane cutting through the object or not respecting the minimum threshold distance.

consideration. We then used the A* graph search algorithm to generate the dexterous manipulation paths for different randomly chosen initial and final configurations. After selecting a random initial configuration, the accessibility of each of the four probes was calculated based on the direction of the rotation axis and the orientation of the object. The potential

Table 2: Graph properties for Object (b) to study the impact of adhesion.

Object (b)	Graph $\mathcal{G}_3$	Graph $\mathcal{G}_4$
Sampling	Octasampling	
Adhesion	Without adhesion	With adhesion
Nodes	544 769	
Rotation edges	2 065 245	
Re-grasping edges	4 631 734	581 524

Table 3: Sampling impact on the trajectories of Object (a).

Metric	Graph	Average	Min	Max	STD
Distance (rad)		2.04	0.83	3.06	0.77
Rotation cost (rad)	$\mathcal{G}_1$	3.23	1.34	6.41	1.51
	$\mathcal{G}_2$	3.61	1.89	6.89	1.53
Finger gaiting cost (rad)	$\mathcal{G}_1$	2.69π	1π	3π	0.63π
	$\mathcal{G}_2$	3π	2π	4π	0.70π
Total cost (rad)	$\mathcal{G}_1$	11.69	4.89	15.83	3.02
	$\mathcal{G}_2$	13.04	8.17	16.73	3.08
Time (s)	$\mathcal{G}_1$	621.55	9.62	2315.72	608.32
	$\mathcal{G}_2$	258.71	13.10	1333.48	351.97

Table 4: Adhesion impact on the trajectories of Object (b).

Metric	Graph	Average	Min	Max	STD
Distance (rad)		1.94	0.37	3.12	0.72
Rotation cost (rad)	$\mathcal{G}_3$	3.81	1.46	6.65	1.20
	$\mathcal{G}_4$	4.67	1.46	8.78	1.72
finger-gaiting cost (rad)	$\mathcal{G}_3$	2.73π	0π	4π	0.98π
	$\mathcal{G}_4$	4.82π	0π	10π	2.3π
Total cost (rad)	$\mathcal{G}_3$	12.40	1.46	17.99	3.78
	$\mathcal{G}_4$	19.82	1.46	38.47	8.48
Time (s)	$\mathcal{G}_3$	391.81	0.42	2804.32	631.45
	$\mathcal{G}_4$	75.28	0.31	378.86	95.37

initial grasps were then identified by considering the stable grasps under the accessibility constraints. Each potential initial grasp was evaluated for probe-probe collision during the first step of the manipulation. We generated 30 random initial and final configurations and planned the trajectories using $\mathcal{G}_1$ and $\mathcal{G}_2$. The simulation results obtained (actual distance between the configurations, path costs separated into rotation and finger-gaiting costs, and computational time) are reported in Table 3.

In terms of path cost, $octasampling$ generated paths that were on average 1.1 times more costly than those generated by $icosampling$. Decomposing the cost difference into rotation and finger-gaiting costs, we observed that the percentage increase in both was equal. We can therefore deduce that the costs of the paths are not heavily impacted by the choice of sampling method. The cost saving of $icosampling$ compared to $octasampling$ was relatively low.

However, in terms of computational time, $octasampling$ was on average 2.4 times faster than $icosampling$, which makes it significantly more appealing.

5.3 Impact of Adhesion on the Graphs and the Paths

Based on $octasampling$, we built two graphs for Object (b), $\mathcal{G}_3$ and $\mathcal{G}_4$, considering respectively the cases without adhesion and with adhesion (worst-case scenario). As reported in Table 2, the number of nodes and rotational edges in the graphs $\mathcal{G}_3$ (without adhesion) and $\mathcal{G}_4$ (with adhesion) is the same. However, $\mathcal{G}_3$ (without adhesion) contains more re-grasping edges compared to $\mathcal{G}_4$ (with adhesion). The reason is the worst-case scenario we considered in the presence of adhesion forces, where the grasps must be able to counteract the pull-off force induced by the overestimated adhesion of the probe to be detached. Consequently, only the grasps able to counteract this force lead to an edge in $\mathcal{G}_4$ (with adhesion).

To analyse the impact of adhesion, we generated 30 random initial and final configurations and planned the trajectories using $\mathcal{G}_3$ and $\mathcal{G}_4$. The results are presented in Table 4. Note that the average cost of the paths without adhesion was 12.4 rad, while with adhesion, it was 19.82 rad. Therefore, on average, the path cost while considering the worst-case scenario in the presence of adhesion is 1.6 times higher than without adhesion. However, if we separately compare the rotation cost and the finger gaiting cost in both graphs, we note that the average rotation cost increased by only 1.2 times, while the average finger gaiting cost increased by 1.7 times when taking adhesion into consideration. This is because finger gaiting is a costly operation and is used more frequently when considering the worst-case scenario. In cases where no finger gaiting steps were used in both generated trajectories, the path cost was the same with and without adhesion.

Regarding the computational time, it is significantly lower (5.2 times lower) when adhesion is taken into consideration. Indeed, manipulation planning without adhesion takes an average of $391.81s$ to find a path, while with adhesion, it takes $75.28s$. This is due to the significant difference in the number of re-grasping edges in both graphs, where $\mathcal{G}_3$ has $4.63 \cdot 10^6$ re-grasping edges, while $\mathcal{G}_4$ has $0.58 \cdot 10^6$.

Illustrations of two paths with the same initial and final configuration, generated with $\mathcal{G}_3$ and $\mathcal{G}_4$, are shown in Fig. 13 and Fig. 14, respectively. Even though both paths start with the same finger gaiting and rotation steps (Fig. 13.a-d and Fig. 14.a-d), they continue with different sequences of 3D rotations and finger gaiting steps. Additionally, trajectory $\mathcal{T}_4$, illustrated in Fig. 14, includes 3 finger gaiting steps, while $\mathcal{T}_3$, illustrated in Fig. 13, has only 2. The difference in trajectories, in terms of rotations and finger gaiting, can be explained by the edges linking the nodes in each of the graphs $\mathcal{G}_3$ and $\mathcal{G}_4$, due to the presence of the pull-off force induced by the adhesion of the detached probe in $\mathcal{G}_4$. The final paths for any manipulation, including translations and rotations, are obtained by superimposing the rotation and translation paths. As a reminder, the translation paths are obtained by simultaneously translating all the probes.

6 Conclusion

In this work, we introduced a novel framework of four co-micromanipulation probes for complex 3D objects that takes into account adhesion forces, probe-object accessibility,

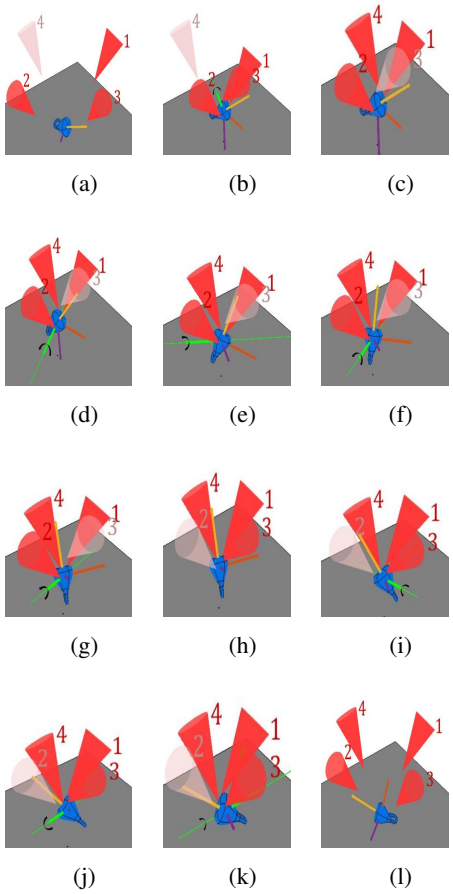

Fig. 13: Illustration of the trajectory without pull-force on the contact points. (a) Initial configuration; (b) Rotation with probes 1, 2 and 3; (c) Adding probe 4 and detaching probe 3; (d)-(g) Successive rotations with probes 1,2 and 4; (h) Adding probe 3 and detaching probe 2; (i)-(k) Successive rotations with probes 1,3 and 4; (l) Final configuration

and probe-probe collisions. This is the first framework applicable to dexterous 3D micro-manipulation of complex objects. We considered a worst-case scenario where the adhesion forces are null when they contribute to the stability of the grasp and maximal when they disturb it. This original strategy allows the generation of robust micro-manipulation paths in the presence of uncertain and varying adhesion forces. Optimal micro-manipulation paths were obtained by exploring the graph with the A* algorithm. Another contribution of this work is a new, efficient sampling variation of Geodesic DGGS, namely $octasampling$, which is more homogeneous in terms of orientation distribution and relates several rotations to the same rotation axis. The efficiency of this sampling method was demonstrated through: i) the significant decrease in computational time compared to the slight increase in path costs; ii) the high number of rotations generated by the same rotation axis; and iii) the low standard

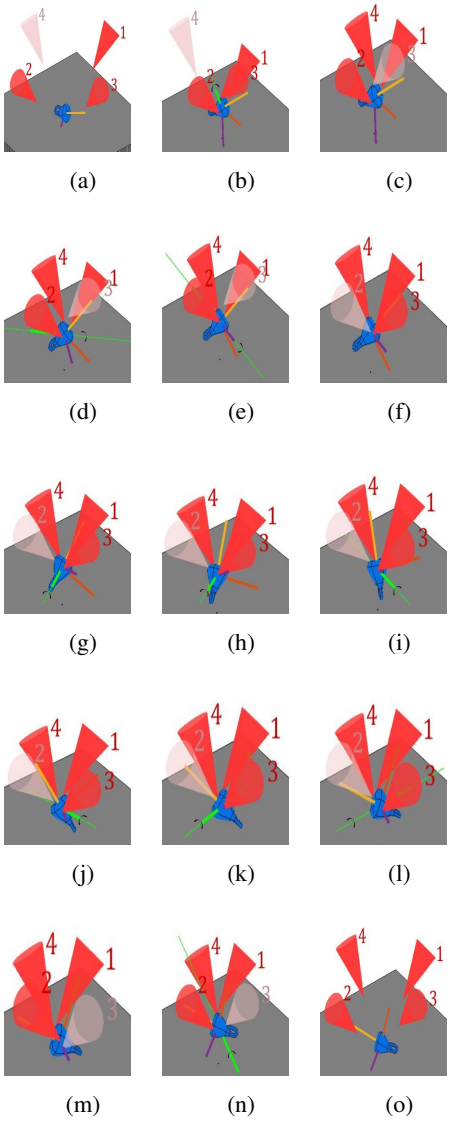

Fig. 14: Illustration of the trajectory with pull-off force on the contact points. (a) Initial configuration; (b) Rotation with probes 1, 2, and 3; (c) Adding probe 4 and detaching probe 3; (d)-(e) Successive rotations with probes 1, 2, and 4; (f) Adding probe 3 and detaching probe 2; (g)-(l) Successive rotations with probes 1, 3, and 4; (m) Adding probe 2 and detaching probe 3; (n) Rotation with probes 1, 2, and 4; (o) Final configuration.

deviation between the orientations when compared to other sampling methods. The simulation results showed interesting and original dexterous micromanipulation trajectories with

enhanced performance. Future work will focus on the experimental validation of the proposed framework.

Supplementary Information. The online version of this article contains a video file that shows the simulation of the micromanipulation with and without adhesion for Object (a) and Object (b) using the four probes.

Acknowledgements. This work was supported by the French ANR program MiniSoRo (ANR-19-CE10-0004), Equipex probeEX network (ANR-10-EQPX-44-01), and EUR EIPHI program (ANR-17-EURE-0002).

References

[1] Tiwari, B., Clevy, C., Lutz, P.: Analysis of Forces during UV Glue Curing for Micro-Assembly Applications. In: 2019 Symposium on Design, Test, Integration & Packaging of MEMS and MOEMS (DTIP), pp. 1–6. IEEE, ??? (2019). https://doi.org/10.1109/DTIP.2019.8752841

[2] Ye, X., Wu, F., Zhang, Z., Wan, B., Zhao, Y.: Laser scanning confocal image alignment assists sub-micron accuracy micro-assembly. Procedia CIRP **76**, 53–58 (2018) https://doi.org/10.1016/j.procir.2018.01.017

[3] Sha, X., Sun, H., Zhao, Y., Li, W., Li, W.J.: A Review on microscopic visual servoing for micromanipulation systems: Applications in micromanufacturing, biological injection, and nanosensor assembly. Micromachines **10**(12) (2019) https://doi.org/10.3390/mi10120843

[4] Zhang, X., Rogowski, L.W., Kim, M.J.: 3D Micromanipulation of Particle Swarm Using a Hexapole Magnetic Tweezer. In: 2019 IEEE/RSJ International Conference on Intelligent Robots and Systems (IROS), pp. 1581–1586. IEEE, ??? (2019). https://doi.org/10.1109/IROS40897.2019.8968300

[5] Zhang, Z., Wang, X., Liu, J., Dai, C., Sun, Y.: Robotic Micromanipulation: Fundamentals and Applications. Annual Review of Control, Robotics, and Autonomous Systems **2**(1), 181–203 (2019) https://doi.org/10.1146/annurev-control-053018-023755

[6] Pinan Basualdo, F., Misra, S.: Collaborative magnetic agents for 3d microrobotic grasping. Advanced Intelligent Systems **5** (2023) https://doi.org/10.1002/aisy.202370058

[7] Jiang, J., Yang, L., Hao, B., Xu, T., Wu, X., Zhang, L.: Automated microrobotic manipulation using reconfigurable magnetic microswarms. IEEE Transactions on Robotics **PP**, 1–20 (2024) https://doi.org/10.1109/TRO.2024.3428429

[8] Cheng, K., Guo, J., Fu, Y., Guo, J.: Active microparticle manipulation: Recent advances. Sensors and Actuators A: Physical **322**, 112616 (2021) https://doi.org/10.1016/j.sna.2021.112616

[9] Al-Nuaimi, I.I.I., Mahyuddin, M.N., Bachache, N.K.: A non-contact manipulation for robotic applications: A review on acoustic levitation. IEEE Access **10**, 120823–120837 (2022) https://doi.org/10.1109/ACCESS.2022.3222476

[10] Basualdo, F.N.P., Bolopion, A., Gauthier, M., Lambert, P.: Solving the non-linear motion in a micromanipulation system powered by thermocapillary flows. IEEE Robotics and Automation Letters **8**(8), 4785–4790 (2023) https://doi.org/10.1109/LRA.2023.3288378

[11] Wu, Z., Xu, Q.: Survey on recent designs of compliant micro-/nano-positioning stages. Actuators **7**, 5 (2018) https://doi.org/10.3390/act7010005

[12] Nadour, H., Grayeli, A.B., Poisson, G., Belharet, K.: Cochlerob: Parallel-serial robot to position a magnetic actuator around a patient's head for intracochlear microrobot navigation. Sensors **23**(6), 2973 (2023) https://doi.org/10.3390/s23062973

[13] Leveziel, M., Haouas, W., Laurent, G.J., Gauthier, M., Dahmouche, R.: Migribot: A miniature parallel robot with integrated gripping for high-throughput micromanipulation. Science Robotics **7**(69), 4292 (2022) https://doi.org/10.1126/scirobotics.abn4292

[14] Morgan, A.S., Hang, K., Wen, B., Bekris, K., Dollar, A.M.: Complex in-hand manipulation via compliance-enabled finger gaiting and multi-modal planning. IEEE Robotics and Automation Letters **7**(2), 4821–4828 (2022) https://doi.org/10.1109/LRA.2022.3145961

[15] Piazza, C., Grioli, G., Catalano, M., Bicchi, A.: A century of robotic hands. Annual Review of Control, Robotics, and Autonomous Systems **2**, 1–32 (2019) https://doi.org/10.1146/annurev-control-060117-105003

[16] Savia, M., Koivo, H.N.: Contact micromanipulation - Survey of strategies. IEEE/ASME Transactions on Mechatronics **14**(4), 504–514 (2009) https://doi.org/10.1109/TMECH.2008.2011986

[17] Andrychowicz, O.A.M., Baker, B., Chociej, M., Józefowicz, R., McGrew, B., Pachocki, J., Petron, A., Plappert, M., Powell, G., Ray, A., Schneider, J., Sidor, S., Tobin, J., Welinder, P., Weng, L., Zaremba, W.: Learning dexterous in-hand manipulation. International Journal of Robotics Research **39**(1), 3–20 (2020) https://doi.org/10.1177/0278364919887447

[18] Gupta, A., Yu, J., Zhao, T.Z., Kumar, V., Rovinsky, A., Xu, K., Devlin, T., Levine, S.: Reset-Free Reinforcement Learning via Multi-Task Learning: Learning Dexterous Manipulation Behaviors without Human Intervention. In: 2021 IEEE International Conference on Robotics and Automation (ICRA), vol. 2021-May, pp. 6664–6671. IEEE, ??? (2021). https://doi.org/10.1109/ICRA48506.2021.9561384

[19] Fan, Y., Gao, W., Chen, W., Tomizuka, M.: Real-Time Finger Gaits Planning for Dexterous Manipulation. IFAC-PapersOnLine **50**(1), 12765–12772 (2017) https://doi.org/

10.1016/j.ifacol.2017.08.1831

[20] Falco, P., Attawia, A., Saveriano, M., Lee, D.: On Policy Learning Robust to Irreversible Events: An Application to Robotic In-Hand Manipulation. IEEE Robotics and Automation Letters **3**(3), 1482–1489 (2018) https://doi.org/10.1109/LRA.2018.2800110

[21] Lim, S., Sohn, S.W., Lee, H., Go, G., Choi, H.Y., Park, J.J.: Analysis and evaluation of path planning algorithms for autonomous driving of electromagnetically actuated microrobot. International Journal of Control, Automation and Systems **18**(12), 2943–2954 (2020) https://doi.org/10.1007/s12555-019-0637-9

[22] Kim, C.H., Mak, K.H., Seo, J.: Planning for Dexterous Ungrasping: Secure Ungrasping Through Dexterous Manipulation. IEEE Robotics and Automation Letters **7**(2), 2234–2241 (2022) https://doi.org/10.1109/LRA.2022.3142892 arXiv:2108.13580

[23] Gao, X., Yao, K., Khadivar, F., Billard, A.: Enhancing dexterity in confined spaces: Real-time motion planning for multifingered in-hand manipulation. IEEE Robotics and Automation Magazine **31**(4), 100–112 (2024) https://doi.org/10.1109/MRA.2024.3433110

[24] Cruciani, S., Smith, C., Kragic, D., Hang, K.: Dexterous manipulation graphs. In: IEEE/RSJ International Conference on Intelligent Robots and Systems (IROS), pp. 2040–2047 (2018). https://doi.org/10.1109/IROS.2018.8594303

[25] Lamiraux, F., Mirabel, J.: Prehensile Manipulation Planning: Modeling, Algorithms and Implementation. IEEE Transactions on Robotics **38**(4), 2370–2388 (2022) https://doi.org/10.1109/TRO.2021.3130433

[26] Cappelleri, D.J., Fatovic, M., Shah, U.: Caging micromanipulation for automated microassembly. Proceedings - IEEE International Conference on Robotics and Automation, 3145–3150 (2011) https://doi.org/10.1109/ICRA.2011.5980190

[27] Venkatesan, V., Seymour, J., Cappelleri, D.J.: Micro-assembly sequence and path planning using subassemblies. Journal of Mechanisms and Robotics **10**(6), 1–12 (2018) https://doi.org/10.1115/1.4041333

[28] Seon, J.A., Dahmouche, R., Gauthier, M.: Enhance In-Hand Dexterous Micromanipulation by Exploiting Adhesion Forces. IEEE Transactions on Robotics **34**(1), 113–125 (2018) https://doi.org/10.1109/TRO.2017.2765668

[29] Kumar, P., Gauthier, M., Dahmouche, R.: Path planning for 3-D in-hand manipulation of micro-objects using rotation decomposition. Micromachines **12**(8) (2021) https://doi.org/10.3390/mi12080986

[30] Tchouatat Kepseu, I., Gauthier, M., Dahmouche, R.: Path planning for 3-d in-hand

dexterous micro-manipulation in presence of adhesion forces. In: 2022 IEEE 18th International Conference on Automation Science and Engineering (CASE), pp. 424–430 (2022). https://doi.org/10.1109/CASE49997.2022.9926566

[31] Brazey, B., Dahmouche, R., Seon, J.-A., Gauthier, M.: Experimental validation of in-hand planar orientation and translation in microscale. Intelligent Service Robotics **9** (2015) https://doi.org/10.1007/s11370-015-0183-0

[32] Fernandez, A., Gazeau, J.P., Zeghloul, S., *et al.*: Regrasping objects during manipulation tasks by combining genetic algorithms and finger gaiting. Meccanica **47**(4), 939–950 (2012) https://doi.org/10.1007/s11012-011-9486-1

[33] Seon, J.-A., Dahmouche, R., Gauthier, M.: Enhance in-hand dexterous micromanipulation by exploiting adhesion forces. IEEE Transactions on Robotics **PP**, 1–13 (2017) https://doi.org/10.1109/TRO.2017.2765668

[34] Rossi, A., Barbiero, M., Scremin, P., Carli, R.: Robust visibility surface determination in object space via plücker coordinates. Journal of Imaging **7**(6), 96 (2021) https://doi.org/10.3390/jimaging7060096

[35] Kelner, J.M., Burzynski, W., Stecz, W.: Modeling uav swarm flight trajectories using rapidly-exploring random tree algorithm. Journal of King Saud University - Computer and Information Sciences **36**(1), 101909 (2024) https://doi.org/10.1016/j.jksuci.2023.101909

[36] Kuffner, J.J.: Effective sampling and distance metrics for 3d rigid body path planning. In: IEEE International Conference on Robotics and Automation, 2004. Proceedings. ICRA '04. 2004, vol. 4, pp. 3993–39984 (2004). https://doi.org/10.1109/ROBOT.2004.1308895

[37] Sahr, K., White, D., Kimerling, A.: Discrete global grid system. Cartography and Geographic Information Science - CARTOGR GEOGR INF SCI **30**, 121–134 (2003) https://doi.org/10.1559/152304003100011090

[38] Vishwanath, B., Nanjundaswamy, T., Rose, K.: A geodesic translation model for spherical video compression. IEEE Transactions on Image Processing **31**, 2136–2147 (2022) https://doi.org/10.1109/TIP.2022.3152059

[39] Cao, S., Chen, P., Lu, G., Deng, Y., Zhang, D., Chen, X.: Spherical gravity forwarding of global discrete grid cells by isoparametric transformation. Mathematics **12**(6) (2024) https://doi.org/10.3390/math12060885

[40] Tegmark, M.: An icosahedron-based method for pixelizing the celestial sphere. The Astrophysical Journal **470**(2), 81 (1996) https://doi.org/10.1086/310310

[41] Lei, K., Qi, D., Tian, X.: A new coordinate system for constructing spherical grid systems. Applied Sciences **10**(2) (2020) https://doi.org/10.3390/app10020655

[42] Chalin, D.V., Rochal, S.B.: Landau theory and self-assembly of spherical nanoclusters and nanoparticles with octahedral symmetry. Physical Review B **107**(2) (2023) https://doi.org/10.1103/physrevb.107.024102

[43] Collins, J., Goel, S., Deng, K., Luthra, A., Xu, L., Gundogdu, E., Zhang, X., Vicente, T.F.Y., Dideriksen, T., Arora, H., Guillaumin, M., Malik, J.: Abo: Dataset and benchmarks for real-world 3d object understanding. In: 2022 IEEE/CVF Conference on Computer Vision and Pattern Recognition (CVPR), pp. 21094–21104 (2022). https://doi.org/10.1109/CVPR52688.2022.02045